

Design, characterization, and scale-up of oscillating plasma actuators for turbulent drag reduction

*Original*

Design, characterization, and scale-up of oscillating plasma actuators for turbulent drag reduction / Neretti, Gabriele; Magnani, Lorenzo; Bellani, Gabriele; Cristofolini, Andrea; Popoli, Arturo; Talamelli, Alessandro; Serpieri, Jacopo. - In: SENSORS AND ACTUATORS. A, PHYSICAL. - ISSN 0924-4247. - (In corso di stampa). [10.1016/j.sna.2026.117952]

*Availability:*

This version is available at: 11583/3010588 since: 2026-05-06T07:56:26Z

*Publisher:*

Elsevier

*Published*

DOI:10.1016/j.sna.2026.117952

*Terms of use:*

This article is made available under terms and conditions as specified in the corresponding bibliographic description in the repository

*Publisher copyright*

Elsevier postprint/Author's Accepted Manuscript

© 9999. This manuscript version is made available under the CC-BY-NC-ND 4.0 license  
<http://creativecommons.org/licenses/by-nc-nd/4.0/>. The final authenticated version is available online at:  
<http://dx.doi.org/10.1016/j.sna.2026.117952>

(Article begins on next page)

## Graphical Abstract

### **Design, characterization, and scale-up of oscillating plasma actuators for turbulent drag reduction**

Gabriele Neretti, Lorenzo Magnani, Gabriele Bellani, Andrea Cristofolini, Arturo Popoli, Alessandro Talamelli, Jacopo Serpieri

## Highlights

### **Design, characterization, and scale-up of oscillating plasma actuators for turbulent drag reduction**

Gabriele Neretti, Lorenzo Magnani, Gabriele Bellani, Andrea Cristofolini, Arturo Popoli, Alessandro Talamelli, Jacopo Serpieri

- High-spatiotemporal-resolution analysis of the transient discharge phases of oscillating plasma actuators
- Up-scaling of oscillating plasma actuators for controlling high Reynolds number flows

# Design, characterization, and scale-up of oscillating plasma actuators for turbulent drag reduction

Gabriele Neretti<sup>a</sup>, Lorenzo Magnani<sup>b</sup>, Gabriele Bellani<sup>b</sup>, Andrea Cristofolini<sup>a</sup>, Arturo Popoli<sup>a</sup>, Alessandro Talamelli<sup>b</sup>, Jacopo Serpieri<sup>c</sup>

<sup>a</sup>*Department of Electrical, Electronic and Information Engineering “Guglielmo Marconi”, University of Bologna, Bologna, 40136, Italy*

<sup>b</sup>*Department of Industrial Engineering (DIN), University of Bologna, Forlì, 47121, Italy*

<sup>c</sup>*Department of Mechanical and Aerospace Engineering (DIMEAS), Politecnico di Torino, Turin, 10129, Italy*

---

## Abstract

In this article, we present the design of an array of plasma actuators (PAs) conceived to control turbulent wall-bounded flows and a unique characterization of its transient response. The actuator configuration is such as to induce a control flow oscillating along the spanwise direction aimed at reducing skin-friction in turbulent flows when tuned to the proper spatio-temporal scales. A full characterization of the transient behavior of the spatio-temporally evolving plasma discharges was carried out by high-speed Schlieren imaging, capturing up to 10 000 density/temperature gradient fields per second. From these images, the evolution of the plasma-induced flow was tracked with sub-millisecond temporal resolution and sub-millimeter spatial resolution, and the actuator performance was evaluated over a wide range of operating conditions. In addition to the characterization of the transient flow, several other relevant quantities were measured and reported: the average jet velocity, the electric power absorption, the plasma-OFF and plasma-ON PA capacitance, and the induced temperature of/from the considered plasma actuators/discharge. Finally, scaling arguments on actuator and power-electronics are presented and discussed as part of a design effort to install the array of oscillating plasma actuators in large-scale facilities able to reproduce flow regimes of interest for transport applications (e.g. aeronautical), such as the turbulent pipe flow facility in the CICLoPE laboratory.

*Keywords:* Plasma Actuators, Turbulent Drag Reduction, Experiments

---

<b>List of Acronyms</b>	HV 1/2 High Voltage (electrode) 1 or 2, see Fig.3
AC Referring to the AC signal	LP Long Pipe
AFC Active Flow Control	OPA Oscillating Plasma Actuator
CICLoPE Centre for International Cooperation in Long Pipe Experiments	OPA-A Oscillating Plasma Actuator Array
DBD Dielectric Barrier Discharge	PA Plasma Actuator
EHD Electro-Hydrodynamic	PIF Plasma-Induced Flow
GND Ground	PIV Particle Image Velocimetry
	SPA Single Plasma Actuator

## 1. Introduction

### 1.1. Context

It is well known that skin-friction drag caused by turbulence is responsible for a large portion of the energy consumption, and therefore pollution, of transport vehicles such as: airplanes (50% of total drag), ships (80%) and conventional high-speed trains (30%) [1, 2, 3].

Possible strategies to reduce friction drag rely either on *passive* approaches, usually based on the installation over the flow exposed surfaces of peculiar geometries (riblets, ridges, shark-skin, dimples, etc.) or *active* methodologies (see the review articles [4, 5]). Due to their inherently robust configurations, passive flow control techniques are increasingly being adopted in the market. However, they still require some maintenance due to the wearing off caused by atmospheric agents, fowling and/or debris. Moreover, the theoretical maximum levels of drag reduction they can achieve caps to  $\approx 10\%$  for lab-scale flows and much lower values, if not drag enhancement, are attained for their off-design employment [4, 5]. On the contrary, active flow control (AFC) approaches have the advantage of being potentially more effective (overcoming 40% in drag reduction) and more adaptable at various flow conditions. However, the inherent power cost related to their operation should be quantified and overcome by the attained power saving [1, 4, 5].

A very effective technique to reduce friction drag produced by turbulent flows exploits spanwise wall-oscillations (e.g. [6, 7, 8]). The wall oscillations introduce a spanwise laminar flow modulation at the wall (analytically

described by Stokes' second problem and known as Stokes' flow), that shelters the wall from the higher drag events (sweeps) related to the bursting of turbulence coherent structures and reduces their intensity [1, 9]. However, implementing spanwise movable parts on actual vehicle surfaces is unfeasible; therefore, a suitable technology must be able to reproduce the same effect without moving parts.

One of such potential technologies considers arrays of wall-mounted plasma actuators (PAs) (see the review articles [10, 11, 12]) configured to produce a spanwise-oscillating flow analogous to Stokes' flow. The plasma actuators considered for this flow control task are of the dielectric barrier discharge (DBD) type; i.e. featuring a dielectric barrier between the two electrodes where the plasma discharge takes place.

In DBD plasma actuators, plasma, an ionized but globally-neutral gas, is formed when the voltage applied to the electrodes exceeds the breakdown voltage of the gas molecules. Under these conditions, pre-existing free electrons are accelerated by the electric field and, acquiring sufficient energy, collide with neutral molecules: this generates new electrons and positive ions (heavier than electrons). Ions are accelerated by the electric field and, colliding with neutral molecules, transfer momentum to the fluid, giving rise to the electro-hydro-dynamic (EHD) force. This momentum transfer generates the ionic wind, a jet of air tangential to the dielectric surface. The intensity of this flow mainly depends on the applied voltage, the frequency of the electrical signal, the geometry of the electrodes and the dielectric material. The flow topology induced by bursts of plasma-generated jets was thoroughly described in references [13, 14]: due to the principle of continuity and conservation of momentum and because of the no-slip condition imposed by the wall, the plasma induced flow (PIF) tends to induce a vortical structure near the wall, especially when the actuator is activated in a fluid initially at rest. This vortex is generated because the plasma jet entrains the adjacent fluid, creating a circulation that closes by continuity, thus forming a vortex.

In order to generate an oscillatory motion, at least three electrodes are usually considered. These actuators, hereafter referred to as oscillating plasma actuators (OPAs), are typically made of two active electrodes alternatively operated and a passive electrode on the other side of the dielectric layer closing the circuit. More electrodes can be introduced to further increase the spanwise homogeneity of the induced flow, as performed by Hehner et al. [15].

DBD plasma actuators have been used in many studies for friction drag control showing promising results [16, 17, 18, 19, 20, 21, 22, 23, 24, 25, 26,

27, 28, 29]. However, most of these studies did not focus on the transient behavior of plasma actuators and are limited to low-Reynolds number applications. The transient behavior is particularly important as, to induce oscillatory motions, the plasma discharges directed along alternating spanwise directions are modulated in time at relatively high frequencies (in the range of 10-100 Hz). In references [30, 31], the authors investigated the effect of the temporal modulation of OPAs. They introduced a cut-off frequency, which corresponds to the modulation frequency at which the two oscillating jets do not have the time to develop and eventually merge generating a wall-normal plume. This effect can be mitigated by increasing the applied voltage or reducing the spacing by two adjacent electrodes. Although this flow forcing could still induce some levels of drag reduction, similar to what was investigated in references [32, 33, 27], it relies on different flow mechanisms compared to the oscillating-wall approach considered in this study. Despite these studies [13, 14, 30, 31], the physical mechanism of the creation of plasma discharge and how energy is transferred to the fluid, not to mention the interaction with the fluid, is still poorly understood; therefore, experimental data on the dynamic behavior of the plasma-induced flow is needed.

The applicability of OPAs for friction drag reduction in higher Reynolds ( $Re$ ) number flows is also an open problem both from the fluid dynamics and the electric perspective. In a turbulent flow, the Reynolds number can be seen as the ratio between the largest and the smallest spatio-temporal scales. In particular, the reference parameter adopted when dealing with skin-friction drag caused by turbulence is the friction Reynolds number,  $Re_\tau$ , that is the Reynolds number based on the friction velocity,  $u_\tau$ . This requires strict specifications on the actuator design, both in terms of actuator spacing and of excitation time-scales.

Narrowly-spaced time-lagged high voltage electrodes are not easy to fabricate and to operate due to the electric interactions among them [34], and the fluid dynamic mutual influence among the induced jets [30, 31]. Moreover, fast temporal modulations can lead to the previously described wall-normal plumes. In this regard, the recently introduced concept of outer scale actuation (OSA), where the targeted turbulence structures are those further away from the wall— thus larger spatio-temporal scales— proposed by Marusic et al. [35] and Chandran et al. [36], opens interesting possibilities for the active control of aeronautical flows. This extends also to plasma-based friction drag control efforts which might suffer from the referred fluid dynamics and electric interactions. Nonetheless, as mentioned, the OSA flow control approach is still debated in the literature as the recent numerical investigation

by Gatti et al. [37] objected its benefits.

Finally, considering larger arrays of OPAs to be deployed for higher- $Re$  applications brings also challenges due to the need of larger supplied powers and of matching the impedance of the electric load with the resonance frequency of the high voltage suppliers.

### 1.2. Current study

In this study, we present the design, fabrication, and characterization of an oscillating plasma actuator and its modular extension into an oscillating plasma actuator array (OPA-A), specifically conceived for application in high-Reynolds-number flows. The innovation of the present work lies in a combined time-resolved experimental characterization of the actuator's dynamic behavior and a design-for-scaling approach. A summary of key studies on DBD plasma actuators is provided in the Supplementary Materials to facilitate comparison with existing literature.

First, we made use of a predominantly qualitative technique to extract quantitative measurements with high temporal and spatial resolution, suitable for the investigation of high-Reynolds-number flows and comparable to that required for such conditions, exceeding that of the techniques employed so far. Indeed, the cited works present phase-averaged velocity fields obtained via stereo or planar PIV, whereas we adopt a different approach (which does not require flow seeding and is inherently qualitative) to characterize the transient phase of discharge ignition and to verify that the wall-parallel induced flow is comparable to the characteristic velocities of the turbulent vortical structures to be controlled in order to reduce skin-friction drag. This capability is particularly relevant for high- $Re$  flows, where resolving fast transient phenomena is essential.

The second innovative aspect concerns the scalability of the actuator design toward high-Reynolds-number applications, extending geometries that have so far been employed only at low Reynolds numbers. The choice of a flexible material (Kapton) and the need to simultaneously power a non-conventional number of electrodes stem from the objective of testing plasma actuators intended for AFC applications inside the Long Pipe (LP) wind tunnel, a unique infrastructure capable of reproducing turbulent pipe flows at Reynolds numbers and physical scales representative of aeronautical applications [38, 39]. Scaling from a small actuator (5 cm) to a large one (200 cm) implies a substantial increase in geometric dimensions and electric capacitance, which in turn requires adjusting the AC frequency of the voltage signal supplied to the PAs for matching load impedance and resonance frequency of the high-voltage suppliers as well as increasing the peak voltage

to maintain comparable thrust levels. This process is non-trivial and demands a dedicated preliminary characterization to assess feasibility, power requirements, and operational limits under high- $Re$  conditions.

The article is organized as follows: in Section 2, we describe the design of the actuator and the used high-voltage equipment; in Section 3, we discuss the employed diagnostics. The main results are then presented in Section 4, whereas the conclusions are reported in Section 5. Finally, in two appendices at the end of the manuscript and in the Supplementary Materials, we give more details on the analyses and methodologies.

## 2. Actuator Design

### 2.1. Layout and specifications of the oscillating plasma actuator module

The OPA module hereby considered is made by two DBD single plasma actuators (SPAs) alternatively producing ionic winds in opposite directions. A 3D sketch of an OPA is depicted in Figure 1. Two active high-voltage electrodes (HV 1 and HV 2) are separated from a passive grounded electrode (GND) by means of a solid dielectric layer. Active electrodes are alternatively driven by modulated AC voltages with the same amplitude and frequency, generating an oscillating induced wind that propagates in the positive and negative plasma-jets directions ( $\pm x$ ).

The supplied high-voltage signals are modulated in time by the step functions shown in Figure 2. When the HV 1 electrode is fed, an ionic wind propagating from left to right is produced. Subsequently, the electrode HV 1 is switched off and HV 2 is turned on, generating an induced wind in the opposite direction (from right to left in the figure). Both electrodes are energized for the same time ( $T_{ON}$ ), producing the same induced oscillating wind in opposite directions. The switch-off time  $T_{OFF}$  was set to 1 ms to avoid surface flashovers between HV electrodes.

The design of the oscillating plasma actuator is fundamentally constrained by the characteristic spatio-temporal scales of wall-bounded turbulent flows at high friction Reynolds numbers ( $1 \times 10^4 < Re_\tau < 4 \times 10^4$ ). In these regimes, turbulent flows encompass a broad range of turbulent structures, from near-wall streaks to large outer-layer motions, each governed by distinct length and time scales.

To interact with the turbulence-producing structures near the wall, the actuator-induced spanwise oscillations must be tuned to the characteristic viscous time and length scales. These are defined by the friction velocity  $u_\tau$  and the kinematic viscosity  $\nu$  through the viscous length scale  $l^* = \nu/u_\tau$  and the viscous time scale  $t^* = \nu/u_\tau^2$ . In particular, the optimal oscillation time

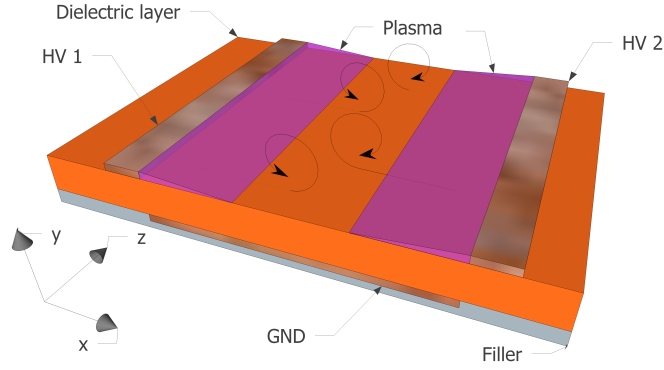


Figure 1: 3D sketch of an oscillating plasma actuator (OPA) and reference axes used in this paper.  $x$ ,  $y$  and  $z$  will also be referred to as spanwise direction, wall-normal direction, and streamwise direction in the manuscript.

is of 100 viscous time scales, although recent studies suggest that targeting the large-scale motion (i.e.  $O(100-1000)$  viscous time scales) might be more effective and efficient at large Reynolds numbers (see the mentioned OSA approach).

As a result, in dimensional terms, for typical airflows in the considered Reynolds number range,  $u_\tau \approx 1-3$  m/s, and the actuator modulation period must lie in the range  $T_{ON} = 5-80$  ms. This corresponds to modulation frequencies in the range of approximately 10–200 Hz. Furthermore, to guarantee a reasonable control authority, the actuator must generate a flow of at least the same order of magnitude of  $u_\tau$ .

In addition to these constraints dictated by the flow physics, the following criteria must be met:

- **Mechanical flexibility**, to allow adaptation to curved surfaces typical of aeronautic applications
- **Reliability**, the OPA must guarantee full functionality for several working hours
- **Reproducibility**, to enable the creation of an OPA array (OPA-A) composed of multiple OPA
- **Scalability**, to cover larger surfaces (e.g. deployment on large test surfaces such as those of the Long Pipe in CICLoPE laboratory)

Regarding the proposed OPA, flexibility and reliability were guaranteed by adopting a 400  $\mu\text{m}$  thick Kapton layer as dielectric material. This polymer

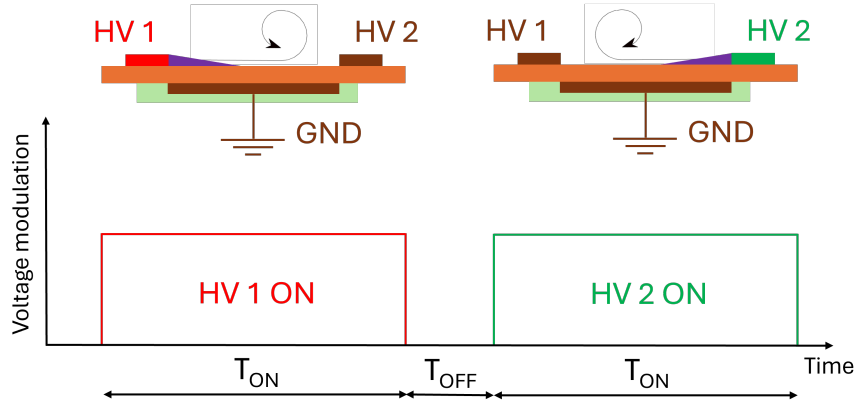


Figure 2: Layout and operating principle of an oscillating plasma actuator (OPA) module: when HV 1 is supplied, an ionic wind is produced from left to right; when HV 2 is ignited, the ionic wind propagates from right to left.

has a dielectric strength exceeding  $100 \text{ kV mm}^{-1}$ , is chemically stable and can be continuously subjected to temperatures up to  $240 \text{ }^\circ\text{C}$  without changing its main properties, while the thin layer thickness allows the OPA to be adapted to curved surfaces.

The availability of a  $0.5 \text{ m}$  large,  $5 \text{ m}$  long Kapton roll, makes it possible to create OPA-As with a curvature compatible with the cylindrical shape of the surface in the CICLoPE wind tunnel or other curved surfaces (e.g. the surface of a wing or fuselage). Furthermore, Kapton-based plasma actuators of this type can produce a wall jet with a maximum velocity of about  $4 \text{ m/s}$  (see reference [40]), thus guaranteeing control authority.

The electrodes were manufactured using a  $80 \text{ }\mu\text{m}$ -thick copper tape foil, which was attached to the dielectric surface using an adhesive layer. To enhance durability and avoid the creation of unwanted discharges, the encapsulated electrodes were insulated with a cast of epoxy resin.

## 2.2. Design of the oscillating plasma actuator array (OPA-A)

While a single OPA module is capable of generating spanwise oscillatory forcing, it is insufficient to provide uniform wall forcing over extended surfaces as required [15], especially in realistic high-Reynolds number flow control applications. Therefore, a modular OPA-A is introduced, as shown in Figure 3: it is constituted by eight OPAs, each with a length of  $25 \text{ cm}$ , yielding a total plasma length of  $8 \times 25 \text{ cm} = 200 \text{ cm}$ . The transition to an array configuration introduces a set of additional design constraints.

More specifically, the dimension of the exposed high voltage electrodes,  $a$ , must be large enough to avoid the formation of plasma discharges between the encapsulated electrodes and the furthest edge of the exposed electrodes (also referred to as “back plasma”). This unwanted discharge phenomenon produces an induced wind in the opposite direction to the desired one, thus limiting the effect of the OPA. Furthermore, the width of the ground electrodes,  $b$ , and consequently the distance between the two active electrodes HV 1 and HV 2 must be large enough to guarantee a full development of the plasma front and to avoid a direct surface discharge between the two exposed HV electrodes for the whole considered range of input voltages (see also the approach to this problem discussed in [34]). Previous studies showed that reducing the width of the ground electrode (lower values of  $b$ ) can lead to the formation of surface flashover, probably due to the presence of a large amount of charges deposited onto the dielectric surface by plasma action [41].

Taking these aspects into account, the geometric dimensions for the present application were chosen as (see Fig. 3):

- Exposed high-voltage electrode width:  $a = 3$  mm, chosen to suppress undesired back discharges at 4.5 kV
- Ground electrode width:  $b = 9$  mm, large enough to accommodate full plasma front development and prevent direct discharges between HV 1 and HV 2
- Inter-module spacing:  $c = 6$  mm, to avoid electrical interaction between adjacent OPAs in the array

A complete characterization of the OPA modules was performed to make sure that the actuator with the described layout can be operated in the range of 0-4.5 kV without surface flashovers or other unwanted discharges, while providing a PIF with the desired characteristics.

### 2.3. High voltage power supply

The OPA-A was supplied by a dual-phase, high-voltage sinusoidal power supply based on the architecture described in references [42, 43]. An Arduino DUE micro-controller managed the power electronics connected to an AC-DC converter, feeding two flyback transformers. In this way, two separated high-voltage signals were generated. Each phase was automatically switched on alternatively, for a time interval equal to the selected  $T_{ON}$  (see Figure 2). The maximum available average power of each phase was equal to 300 W.

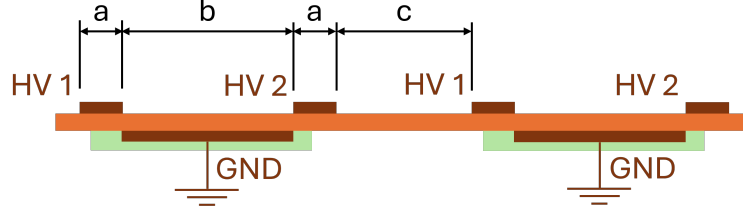


Figure 3: Two out of eight Oscillating Plasma Actuators (OPAs), constituting part of an Oscillating Plasma Actuator Array (OPA-A), each with a length of 25 cm (total plasma length:  $8 \times 25 \text{ cm} = 200 \text{ cm}$ ).  $a = 3 \text{ mm}$ ,  $b = 9 \text{ mm}$ ,  $c = 6 \text{ mm}$ .

The amplitude and frequency of the voltage waveform were varied in the range 3.5-6 kV and 12-31 kHz, respectively. These voltage variations were necessary to ensure impedance matching between power supply and load (OPA-A), and to characterize the OPA-A performance.

### 3. Experimental setup and methods

#### 3.1. Electrical measurements

The applied voltage was measured using two Tektronix P6015A high-voltage wide-band probes (one for each phase). The average power feeding the discharge was evaluated using the capacitor method or the Lissajous-figure method [44], analyzing the charge-voltage characteristics of the actuator. The figure obtained by plotting the instantaneous charge  $Q(t)$  as a function of the instantaneous applied voltage  $v_m(t)$ , is useful for diagnosing the electrical properties of DBD actuators [45]. The area enclosed by the  $Q - v_m$  diagram corresponds to the energy delivered to the discharge within a cycle [44] and the average power can be defined as:

$$P_{\text{average}} = \frac{1}{T_{AC}} \oint v_m(t) dQ(t) \quad (1)$$

where  $T_{AC}$  is the period of the applied AC voltage. The charge  $Q(t)$  transferred to the actuator was evaluated by measuring the voltage  $v_m(t)$  across a 100 nF measurement capacitor  $C_m$  connected between the buried electrode and the ground reference terminal.

The significantly higher capacitance value of  $C_m$  compared to the actuator's equivalent capacitance ensures that the majority of the high voltage is effectively applied to the actuator electrodes. The relation between transferred charge and measurement capacitor voltage is

$$Q(t) = C_m v_m(t) \quad (2)$$

Applied voltage and current feeding the discharge as a function of time, have been acquired as well. As far as these data were not useful for the paper purposes, a typical voltage-current time behavior has been reported in the Supplementary Material.

### *3.2. Plasma-induced thermal and mean flow measurements*

The steady-state induced jet velocity profiles generated by the single plasma actuator (SPA) were measured using a glass Pitot tube with an outer diameter of 1 mm. The tube was positioned at a distance of 2 mm downstream of the plasma region end onto the dielectric surface and was moved by a step motor with a linear resolution of 0.03 mm. A DCAL401 Sursense ultra-low differential pressure sensor was used to detect pressure variations produced by the wall jet. The acquired signals were filtered by using a digital low-pass filter with a cut off frequency of 100 Hz. All electrical signals were acquired by means of a Yokogawa DL1740 scope with a sample rate of  $10^9$  samples per second.

The actuator surface temperature was measured with a FLIR T1020 infrared-thermal camera. The emissivity set in this instrument was chosen by consulting the literature related with the typical values found for the Kapton material. The temperature of the actuator thermalized with the surrounding ambient was detected by the infrared camera and subsequently compared with the ambient temperature obtained by using a digital thermometer. The difference between the two measurements was found to be within  $0.2^\circ\text{C}$ . The influence of the plasma in the surface temperature measurement was checked by continuously measuring the Kapton temperature with the infrared camera by alternatively switching the plasma ON and OFF. In the instant suddenly after the discharge extinction, no differences were found in the thermal images.

### *3.3. Plasma-induced transient flow measurements*

From the literature, it is known that plasma actuators produce a synthetic wall-parallel flow that develops in the domain. The plasma production process also causes moderate heating of the air surrounding the high-voltage electrode. The Schlieren imaging technique, exploiting the difference in the air refractive index generated by the temperature (and thus density) difference, allows to visualize the plasma-induced flow. Moreover, under the assumption that the temperature field behaves as a passive scalar which evolves under the action of the wall-parallel flow, it is possible to track the PIF, intended as the progression of the front of air warmer than the surrounding ambient air (hot-front), in both time and space.

Combining the Schlieren technique with high-speed imaging, time-resolved measurements on the plasma-induced flow can be performed, allowing for a detailed study of the transient-flow behavior. Images were captured by means of a Z-type configuration Schlieren setup [46]. Illumination was provided by a tungsten halogen low-voltage lamp equipped with a rear reflector. A Schneider-Kreuznach Xenon 40 mm double-Gauss lens with a  $f/1.9$  focal ratio was used as condenser. Two off-axis parabolic mirrors with a diameter of 138 mm and a focal ratio of  $f/3.5$  reflected the light beam. The light beam propagated along the actuator-defined  $z$ -direction (Figure 1). The knife-edge was set perpendicularly to the actuator surface to maximize the detected density gradients, produced by the induced flow.

Images were detected by a high-speed camera Phantom Miro M340, with sensor size of  $2560 \times 1600$  pixels<sup>2</sup>, a pixel size of  $10 \mu\text{m}$ , 12-bits of digital resolution and a maximum frame rate of 800 frames per second at full sensor resolution. The camera was equipped with a SIGMA MACRO DG objective, with a focal length of 180 mm and an f-stop number of 3.5. This allowed us to get the actuator surface in sharp focus. In this configuration, the spatial resolution was of  $0.071 \text{ mm/px}$ . In order to reach a frame rate of 10.000 fps, the resolution was reduced to  $384 \times 512$  pixels<sup>2</sup>. This gives a field of view of approximately  $28 \times 36 \text{ mm}^2$ , which is sufficient to capture the flow in between two electrodes. To reduce the computational effort, images have been further cropped along the  $x$  direction: the resulting field of view is shown in Figure 4.

To assess the evolution in time of the spanwise flow starting from the raw images, two algorithms were implemented: the algorithm used for the PIF tracking, performed by tracing the hot-front, is described in Appendix A; the procedure adopted for the vortex identification and vortex core tracking is reported in Appendix B.

#### 4. Results

The design parameters of the present array of oscillating plasma actuators (OPA-A) were optimized considering the actuator’s electrical and fluid-dynamics performance, while ensuring impedance matching between power supply and electrical load, for both lab-scale and full-scale actuators. In this chapter we report the following results:

- Electrical, thermal and fluid-dynamics characterization of an actuator with a single phase (SPA) consisting of HV 1 and GND electrodes (see Figure 1)

- Fluid-dynamics characterization of the PIF of a lab-scale OPA-A
- Scaling of the performance of a full-scale SPA as compared to a lab-scale actuator

#### 4.1. Single plasma actuator characterization

The first step in designing the OPA-A is the characterization of the SPA, which serves as the foundation for its operation: SPA consists solely of the HV 1 and GND electrodes (see Figure 1). An initial series of tests was conducted to observe the plasma regime and to measure the discharge average power as a function of the applied voltage. An AC voltage signal with a fixed frequency of 30 kHz was selected to ensure effective impedance matching between the high voltage source and the load, and thus a proper operation of the SPA. The tests were conducted for a series of input voltages with a peak amplitude in the range 3.5-5 kV, with increments in steps of 0.5 kV. The results are shown in Figures 5a) and 5b): they show, respectively, the morphology of the plasma discharge together with the plasma extension for the different supplied voltages.

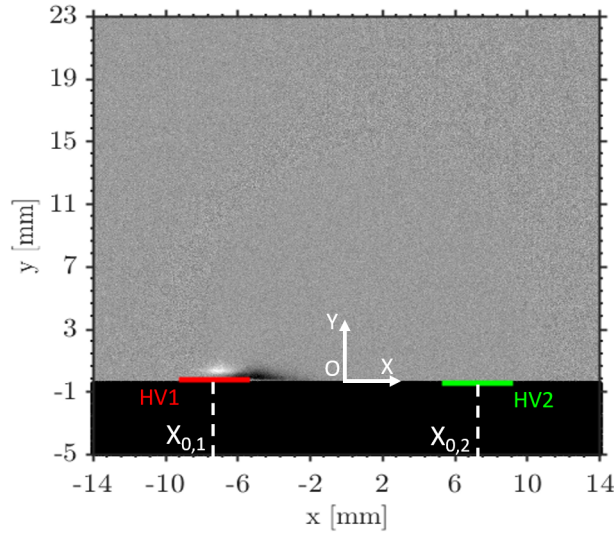


Figure 4: Schlieren image after the background subtraction; in white, the reference system adopted. The high-voltage electrodes HV 1 and HV 2 have been marked with red and green lines, respectively.  $X_{0,1}$  and  $X_{0,2}$  represent the center of HV 1 and HV 2 respectively. Images have been cropped to focus on the region of interest.

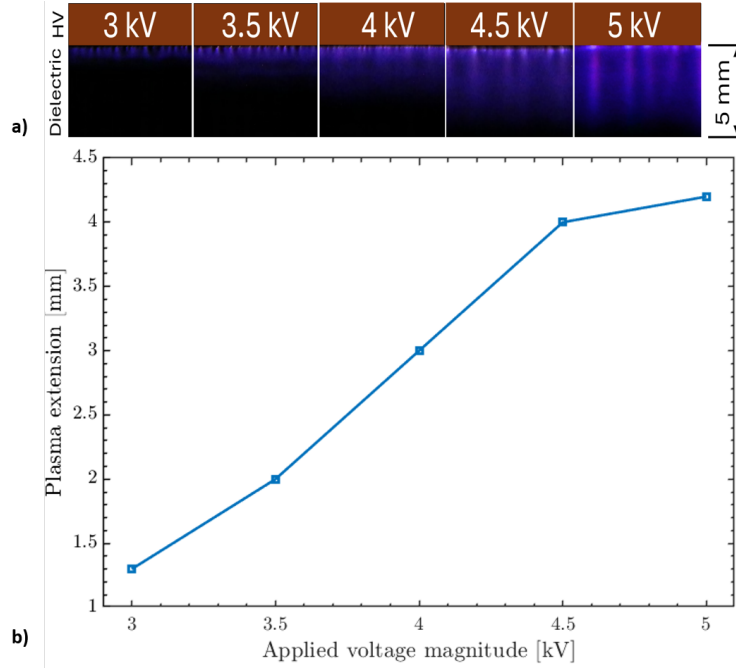


Figure 5: a) Single plasma actuator (SPA) discharge pictures captured with increasing supplied voltages. b) SPA plasma extension for different supplied voltages.

For voltages below 3 kV, the discharge was barely ignited (see Figure 5a)), thus producing a negligible induced wind. For values in the range 3-5 kV, both the induced wind intensity and the plasma extension grew approximately linearly with the applied voltage. For voltages larger than 5 kV, the discharge became strongly non-homogeneous (strong plasma filaments appeared), leading to a large temperature growth and negligible further increments in the plasma length.

Figure 6a) shows the wall mean-velocity profiles induced by the SPA, measured with the glass Pitot tube at a distance of 2 mm downstream of the visible end of the plasma region, for increasing supplied voltages. The obtained wall jet velocity profiles exhibit their highest value close to the actuator surface, with an interaction region spanning a few millimeters. All velocity measurements reported in Figure 6 were obtained by performing an ensemble average over 5 different acquisitions in similar actuation conditions: the relative standard deviations are always within 5%.

As for the plasma extension, the maximum induced velocity increases linearly with the applied voltage, up to 4.5 kV, with limited increments for larger applied voltages (see Figure 6b)). This behavior is related to the

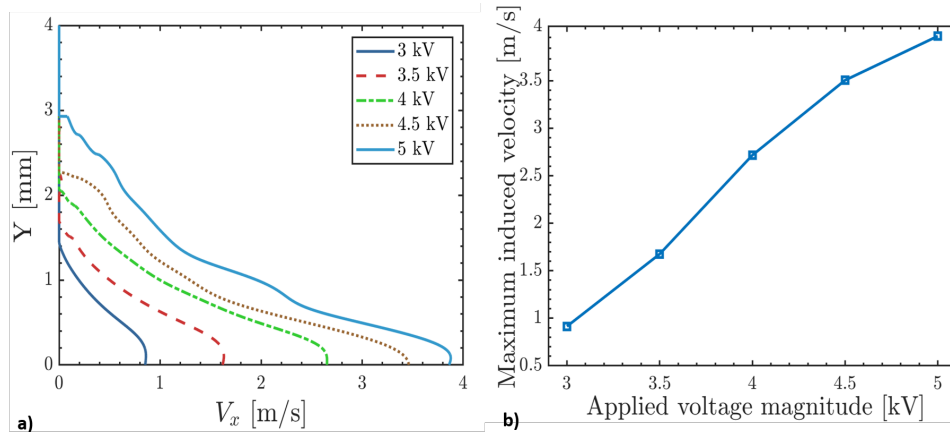


Figure 6: a) Velocity profile induced by the single plasma actuator (SPA), measured 2 mm downstream of the plasma front using a 1 mm-diameter glass Pitot tube at different applied voltages.

limitation in the plasma extension for the largest investigated voltage, and the setting of a strong non-homogeneous discharge. This plasma regime results in a lower conversion efficiency of electric energy into kinetic energy and it is not useful for fluid-dynamics purposes.

In surface DBD actuators, the dielectric surface beneath the discharge filaments experiences a temperature gradient along the plasma propagation direction (i.e. along the  $y$  axis of Figure 1). The highest temperature is observed close to the exposed electrode edge, where plasma formation takes place. For completeness, a thermal image of the SPA supplied with 4.5 kV voltage is provided in the Supplementary Material. These maximum temperature values are useful for assessing the thermal stress on the Kapton surface, as well as the potential fluid-dynamic effects due to buoyancy/viscosity effects.

The temperature increase of the actuator surface is related to the electric average power supplied to the electrodes, which is primarily converted into heat. As previously mentioned, the average power was calculated with the Lissajous figure method for all operating conditions. This allows to evaluate the average power density (W/cm), which is critical for determining the maximum spanwise length of the actuator that can be supported by the power supply. Lissajous figures obtained in all supplying conditions (i.e. by supplying the actuator in the whole voltage range) are reported in the Supplementary Material. An example of Lissajous figure is depicted and explained in Figure 13 .

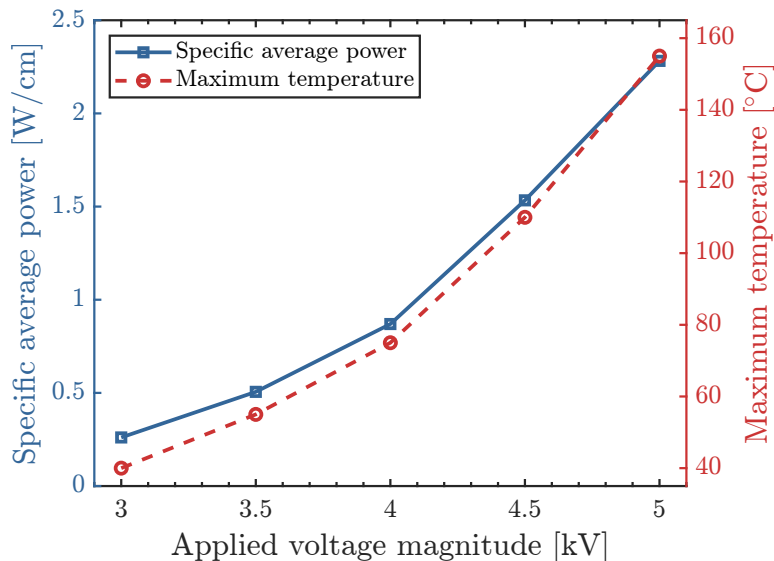


Figure 7: Single plasma actuator (SPA) specific average power and maximum temperature measured for different supplied voltages.

Figure 7 shows the measured specific average power and maximum temperature detected on the surface of the SPA as a function of the applied voltage. These two quantities exhibit similar trends because most of the electrical energy supplied to the actuator is converted into heat [47]. The maximum detected temperature reaches about  $160^{\circ}\text{C}$ . This value is significantly below the maximum continuous working temperature for Kapton ( $240^{\circ}\text{C}$ ). Despite this, the combined effects of temperature and electric field alongside of the corrosive action by the ozone molecules generated in the plasma region, could lead to premature damage of the dielectric layer. Additionally, localized spots with larger temperatures may occur. Furthermore, high temperature values could also cause the detachment of copper electrodes, due to a reduction in the bonding strength of the copper tape glue. For these reasons, to prevent premature actuator failures, a maximum working temperature of  $110^{\circ}\text{C}$  was chosen (see Supplementary Material), corresponding to a specific average power below  $1.5\text{ W/cm}$ . As a consequence, for the future tests reported in this work, a maximum voltage of  $4.5\text{ kV}$  was chosen, corresponding to an induced velocity below  $3.5\text{ m/s}$  (see Figure 6).

#### 4.2. Induced-flow characterization

The previous section shows the results in which the actuators have been operated in a continuous mode; in this section, the plasma actuators were

tested according to the following parameters:

- Modulation period ( $T_{ON}$ ) – from 10 ms to 80 ms. This quantity represents the time interval during which a single HV electrode is powered (see Figure 2). It should not be confused with the period of the sinusoidal voltage waveform that powers the actuator, i.e.,  $T_{AC}$
- Amplitude of the input voltage ( $V_{in}$ ) – from 3.5 to 5 kV
- Frequency of the input voltage ( $f_{AC}$ ) – from 20 to 40 kHz

The images shown from now on will be referred to the following input parameters:  $V_{in}= 4$  kV,  $f_{AC}= 31$  kHz; moreover, unless otherwise specified, all images were acquired with a camera frame rate of 10 kfps.

#### *4.2.1. Transient response of the plasma-induced flow*

Based on the assumption that temperature field behaves as a passive scalar, and by exploiting the integral procedure detailed in Appendix A, the temperature/velocity distribution evaluated at the spanwise location midway between the two exposed electrodes (i.e., at  $X = 0$ ) enables the reconstruction of the wall-normal profiles of the spanwise velocity throughout the oscillation period. To do so, a conversion factor of 0.071 mm/px determined with an optical calibration, is considered to retrieve the displacement and velocity of the propagation front of the PIF in physical units. This procedure allows to assess the structure of the actuator-induced oscillations offering clear support for the introduction of spanwise oscillatory fluid motions.

The velocity profiles, depicted in Figure 8 with solid lines, refer to the actuation case with  $f_M= 100$  Hz. Each profile represents the ensemble average of 10 instantaneous profiles and is smoothed using a Gaussian low-pass filter with a 4-sample window for improved visualization. The interval from 0 to  $\pi$  is defined as the phase during which HV 1 is active, while the interval from 0 to  $-\pi$  corresponds to HV 2 activation. Moreover, the profiles are plotted at increments of  $\pi/5$  to prevent overcrowding of the figure.

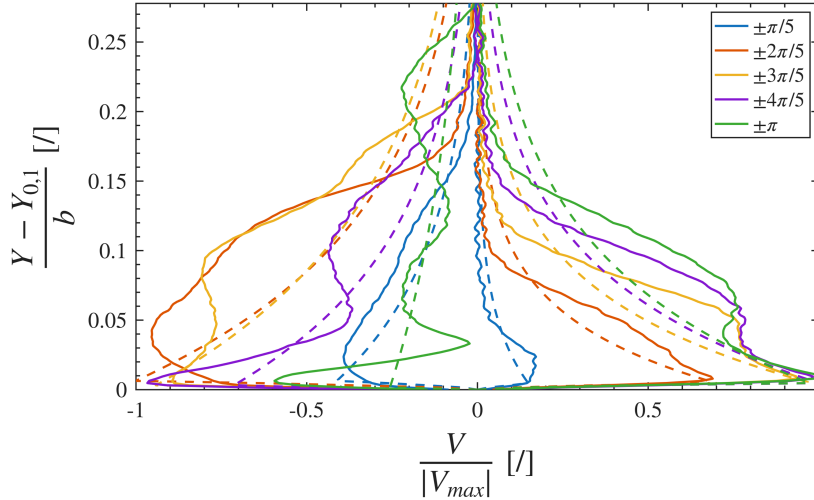


Figure 8: Normalized wall-normal induced velocity profiles acquired at  $X = 0$  and for different phases of the oscillation cycle. Solid lines represent the ensemble average of 10 instantaneous profiles; dashed lines represent the theoretical model based on the momentum equation for 1-D flows.

During the first actuation half-cycle (associated with HV 1), the wall velocity reaches its maximum approximately halfway through the modulation period and subsequently diffuses in the wall-normal direction. When HV 2 is activated, its effect appears as a displacement in the wall-normal direction occurring relatively far from the wall. This behavior is consistent with the upward displacement of the starting vortex induced by the second vortex (i.e. the oppositely-directed one), as also observed in the flow visualizations. Subsequently, the second vortex counteracts the flow moving in the opposite direction, leading to the formation of a second lobe closer to the wall, which is evident in the profiles at  $-4\pi/5$  and  $-\pi$ . Therefore, consistently with the assumptions outlined in Appendix A, the velocity profiles associated with HV 2 appear less confined toward the wall. For comparison, dashed lines are included in the figure, representing the theoretical model proposed by Su et al. [31], which is based on the momentum equation for predominantly one-dimensional flow with a body force.

Moreover, the average displacement and velocity profiles of both HV 1- and HV 2-induced jets along the  $x$  axis for all actuation periods, including the associated maximum deviations, are illustrated in Figure 9.

Figure 9a) suggests that the largest displacement occurs at the very beginning of the gas energization; then the spanwise flow develops in the spanwise direction, progressively decelerating, and a steady state is reached after

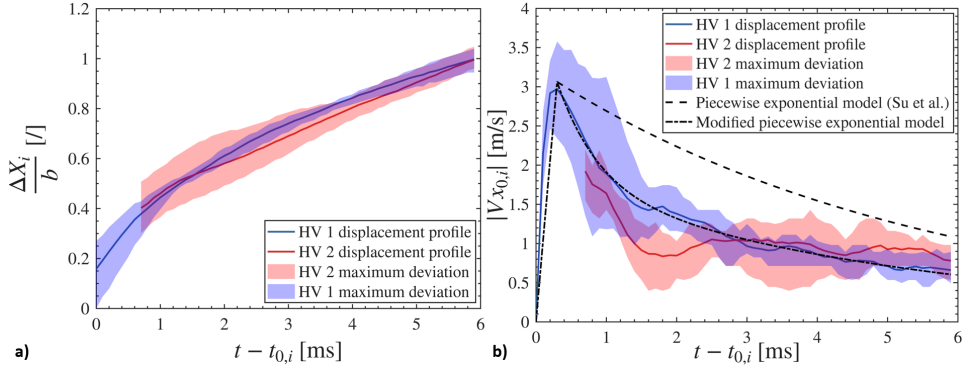


Figure 9: Average profiles (solid lines) of the HV 1- (blue) and HV 2- (red) induced jets for all modulation periods and maximum deviation (shaded regions): a) shows the propagation front of the induced flow; b) delineates the average horizontal velocity profile, where the black dashed line represents the analytical model proposed by [31], whereas the black dash-dot line corresponds to the model proposed in the present work.

approximately 5 milliseconds. Apart from the initial instants after  $t_0$ , a reasonable degree of symmetry between the two phases can be observed. The larger uncertainty associated with HV 2 is mainly due to the development of the spanwise flow in already perturbed air, which increases the uncertainty in the interface detection. Additional discrepancies between the average profiles of the two phases may also arise from slight differences in the copper track layout of the hand-made plasma actuator. The missing portion in the displacement front induced by HV 2 is attributed to the so-called “dead time” occurring between two subsequent modulation periods. As a matter of fact, since the OPA layout is designed to reproduce the effect of an oscillating wall, the two high-voltage electrodes are alternately switched on and off. Consequently, the vortex generated by HV 2 develops in a region previously perturbed by HV 1, i.e. within a flow field characterized by a temperature higher than the ambient one. The dead time, typically of the order of 1 ms, accounts for several factors: the non-instantaneous switching between HV 1 and HV 2, possible non-ideal modulation effects, any parasitic discharge currents arising during phase alternation, and the finite response of the tracking algorithm in detecting the switching between the opposing jets and identifying the maximum in the temperature profile.

Then, knowing the displacement and the time interval between subsequent frames, it is possible to retrieve the velocity profile of the propagation front along the  $x$  axis, whose first actuation period is shown in Figure 9 b).

As expected, the induced flow exhibits a strong initial acceleration, driven

by a sharp and highly localized impulse at the actuator edge. The velocity profile, obtained through a sliding average operation using a 4-sample window (0.4 ms), is similar in shape to that reported by Bolitho and Jacob [48]; however, the velocity induced by the actuators hereby considered is higher. Moreover, the critical frequency identified in that study shows much closer agreement with the results obtained in the present work. The dashed-black curve represents the piecewise exponential model for the time evolution of the spanwise velocity profile proposed by Su et al. [31], where the values of the model have been chosen such to fit with the solid-blue line in Figure 9b). As expected, the decay is initially steep and gradually smooths, with a slower tail—behavior that is not captured by a single-exponential first-order model. The piecewise exponential model reproduces the peak position but fails to match the decay slope. The automatic fit underestimates the peak, reflecting a compromise between the steep rise and slower tail due to the model’s limited two-parameter flexibility. These observations indicate that the system cannot be described as a first-order process. The failure of the piecewise model to capture both the peak and decay implies the presence of multiple characteristic timescales, inertia or nonlinear effects, and transport or accumulation processes that deviate from simple exponential dynamics. Therefore, a different model is proposed, represented by the black dash-dot line in Figure 9b): a modified piecewise exponential formulation characterized by one rise timescale and two decay timescales. The first decay timescale represents the rapid post-peak decrease and is assumed to be equal to the rise timescale, while the second accounts for the slower long-tail relaxation observed in the measurements. In this way, the model captures both the sharp peak formation and the subsequent two-stage decay while retaining a limited number of free parameters. Since the fast decay shares the same characteristic time as the rise, the model effectively introduces only two independent timescales, corresponding to the rapid dynamics and the slower relaxation process.

Finally, it is worth mentioning that these results are in contrast with the experimental results reported in [30, 31], where they show that effective near-wall oscillating flow can only be achieved at a modulation frequency below tens of Hertz. Once beyond this range, the flow pattern transits rapidly from a periodic alternation of two opposite near-wall jets to a quasi-steady vertical jet, resulting in a sharp drop in spanwise oscillation strength. This is not what we observe in our high-speed Schlieren measurements: even at modulation frequencies as high as 100 Hz, we clearly see that the vortex generated by HV 1 and HV 2 is able to cross the entire GND electrode width, and in any case always more than half of it. This is evident both

from the plots in Figure 9a), which describe the displacement of the vortex front, and from the plot in Figure 10a), which shows the displacement of the vortex core.

#### 4.2.2. Vortex-core evolution

For the tracking of the vortex core, a binarization procedure of the measured frames was performed, as described in Appendix B. This method allows to track also the displacement of the propagation front along both the wall-parallel and wall-normal directions. The disadvantage is that following the vortex front after the first modulation period becomes more challenging since the tangential vortex coming from the second high-voltage electrode develops in a region that was already perturbed (thus, warmer) with respect to unperturbed air.

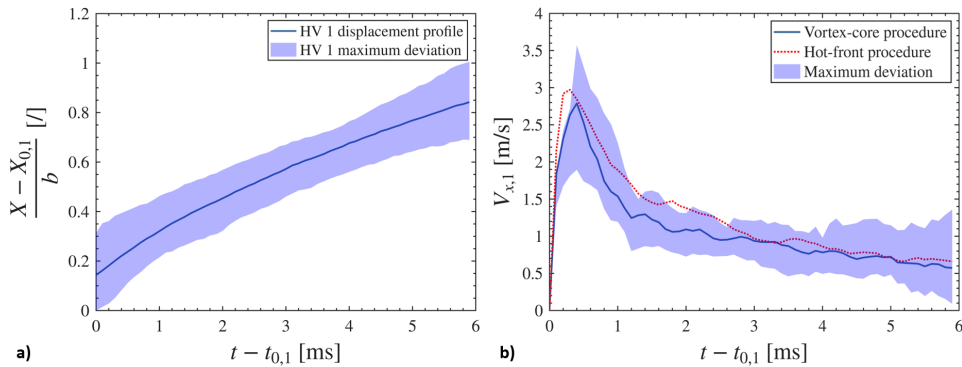


Figure 10: a) Evolution of the vortex core along the  $x$  axis; b) vortex core (blue) and the hot-front (red) velocity profiles from the two different tracking procedures; horizontal average profiles (solid lines) and maximum deviation (shaded regions) from the binarization procedure.

Figure 10a) shows the displacement of the vortex core along the spanwise direction: here, unlike the previous method, the deviation does not decrease as time passes, but stays rather constant during the transient phase. This happens because, as the vortex spreads, the vortex core becomes more sensitive to smaller variations in light intensity: this could be avoided, at least in principle, by setting an adaptive luminosity threshold value. But an algorithm that defines, frame by frame, the brightness level suitable for distinguishing the center of the vortex from other structures is not trivial and could lead to feeble results. Figure 10b) shows the resulting velocity profile: as can be appreciated, in the initial time instants since the discharge onset, the wall-parallel velocity profiles of the vortex center and front are very simi-

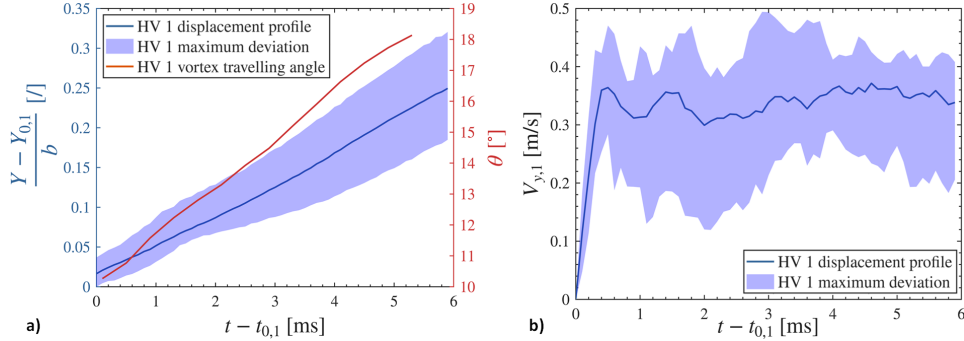


Figure 11: a) Evolution of the vortex core along the  $y$  axis (blue) and of the vortex core travelling angle (red); b) vortex-core vertical velocity profile; vertical average profiles (solid lines) and maximum deviation (shaded regions) from the thresholding procedure.

lar, despite a greater uncertainty compared to the previous technique. Then, the vortex spreads in space and time, causing a velocity difference between the center and the front profiles, with the latter settling at lower velocities. On the other hand, Figure 11 depicts the vortex-core displacement and velocity profile in the wall-normal direction. Even if these profiles represent the evolution of the core of the induced vortex and not of its propagation front, their values confirm the tangential feature of the plasma-induced vortex. Indeed, the development in the  $y$  direction is much slower than in the  $x$  direction.

Moreover, the evolution of the vortex core along the  $x$  and  $y$  axis was exploited to determine the vortex-core travelling angle,  $\theta$ , with the same procedure adopted in reference [13]. As can be verified by examining the corresponding plots, at the very beginning of the energization, the vortex core is characterized by a travelling angle equal to  $10^\circ$ , which monotonically increases up to  $20^\circ$  as the motion becomes affected by diffusion, rather than convection. This is in contrast to what was measured by Mishra et al. [13], which reported a travelling angle of the starting vortex core which is in the range of  $30^\circ$ – $32^\circ$ .

#### 4.3. Oscillating plasma actuator array scale-up

An OPA-A constituted of 8 OPAs with an external size of  $300 \times 150 \text{ mm}^2$  was developed, to be tested in the CICLoPE Long Pipe facility (see Figure 12a) in a future experimental campaign aimed at reducing friction drag for high- $Re$  flows. The equivalent plasma length in the CICLoPE LP is 10 m for each high voltage phase. A total of 5 OPA-As with equivalent active length of 200 cm each will be assembled in the wind tunnel test section (see Figure

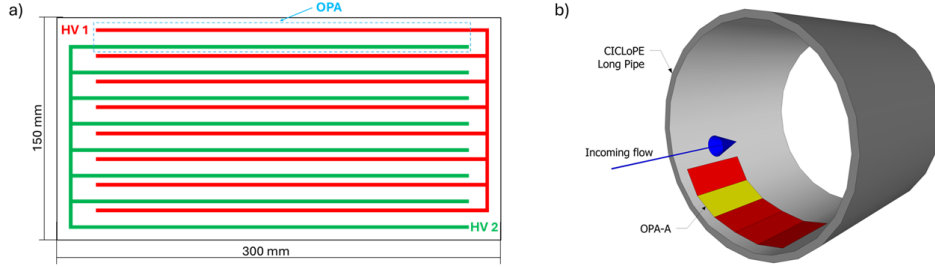


Figure 12: Scheme of the top view of a OPA-A a) and a OPA-A mounted within the CICLoPE test section (diameter 0.9 m).

12b). The specific choice of 200 cm is dictated by the 300 W output average power of the generator, considering a maximum specific average power of 1.5 W/cm.

According to the maximum power transfer theorem, maximum power is delivered when the generator impedance equals the complex conjugate of the load impedance. Therefore, the operating conditions and electrical parameters of the HV generator must be adapted to properly supply the scaled actuator. This aspect is particularly critical in the present system because the HV generator is based on a resonant transformer topology (see reference [42] for details). In such converters, the output voltage strongly depends on the operating frequency relative to the resonance frequency of the generator–load system. Since the actuator behaves predominantly as a capacitive load, scaling the actuator length significantly modifies the equivalent capacitance seen by the generator and consequently shifts the resonance frequency of the system. As a result, the voltage gain of the generator and its optimal operating point may change substantially. For this reason, a circuit-level analysis of the coupled generator–actuator system is required in order to correctly design the scaled configuration.

In this section, the procedure adopted to scale up the single plasma actuator (SPA) to a full-scale oscillating plasma actuator array (OPA-A) is described.

#### 4.3.1. Estimation of the full-scale actuator capacitance

The equivalent capacitance of the OPA-A (full-scale actuator) was estimated by extrapolating the small-scale SPA capacitance measured through the Lissajous method (Figure 13). The SPA is characterized by an equivalent cold capacitance  $C_{OFF}$ , related solely to the actuator geometry when no plasma discharge takes place, and by a higher capacitance value  $C_{ON}$

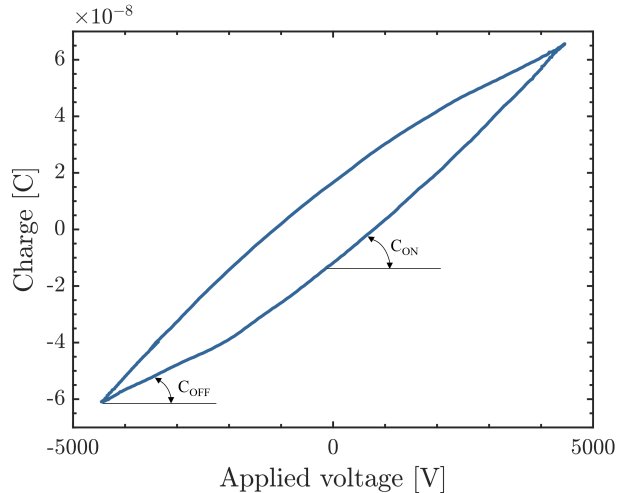


Figure 13: Lissajous figure obtained for the 5 cm SPA actuator supplied with a 4.5 kV.

associated with the ignition of the discharge. Since the plasma remains ignited for most of the AC signal period (about three quarters of it, as also indicated by the capacitance variation in Figure 13),  $C_{ON}$  was selected as the representative equivalent capacitance of the small-scale actuator.

This choice represents a conservative scenario because higher equivalent capacitance values correspond to larger variations in the operating frequency required to achieve the desired performance of the power source. According to the Lissajous measurements reported in Figure 13, the capacitance in plasma-on conditions was found to be  $C_{ON} = 15.1$  pF for the 5 cm SPA, while  $C_{OFF} = 7.5$  pF. Assuming a linear scaling with the actuator length, the equivalent capacitance of the large-scale 200 cm OPA-A is therefore estimated to be approximately 604 pF.

We note that, in plasma-on conditions, an effective resistance must also be introduced in the circuit representation to account for the active power absorbed by the discharge. The numerical value of equivalent resistance was determined by matching the simulated active power to the corresponding experimental measurements.

#### 4.3.2. Validation of the generator-load system equivalent circuit

Using the load parameters discussed in the previous paragraph, and after performing an electrical characterization of the transformer employed in the generator as described in reference [42], an equivalent circuit model of the coupled generator-reactor system was implemented in the LTSpice simula-

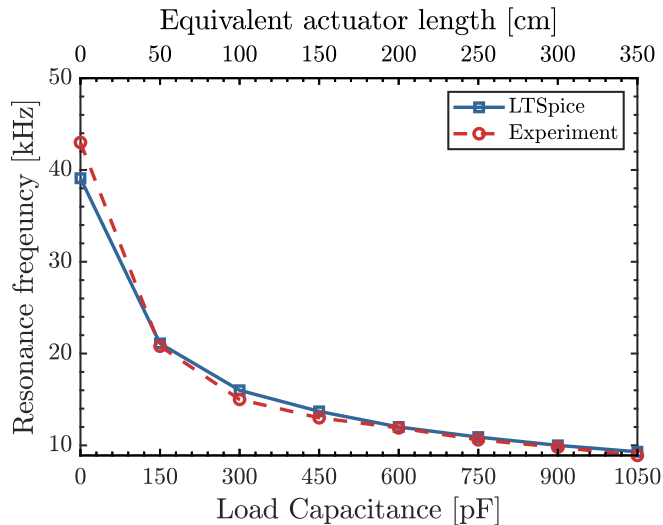


Figure 14: Measured and simulated resonance frequency of the electric system as a function of the load capacitance and equivalent SPA length in cm.

tion environment. The validation of the model was performed by comparing the simulated resonance frequency of the system as a function of the load capacitance with experimental measurements.

The resonance frequency measurements were carried out using a modular capacitive load, adjustable between 0 pF and 1050 pF in steps of 150 pF. The capacitors were manufactured using a 400  $\mu\text{m}$  Kapton layer as dielectric material and copper tape as plates. This capacitance range corresponds to an equivalent SPA streamwise length (see Figure 1) between 0 and approximately 350 cm. The edges of the encapsulated electrodes were filled with silicon to avoid surface plasma formation. The input DC voltage was selected so as to limit the output high voltage when operating close to the resonance frequency. The results of the comparison, reported in Figure 14, show a good agreement, confirming the reliability of the developed equivalent circuit.

#### 4.3.3. Generator operating point adaptation for the scaled actuator

After validating the equivalent circuit of the generator–load system, the model was used to investigate how actuator scaling affects the electrical operating conditions of the generator. In particular, frequency-domain circuit simulations were performed to analyze the frequency response of the coupled generator–reactor system for both the small- and large-scale actuators.

At a constant DC bus voltage (10.8 V in the performed simulations), the maximum achievable output voltage of the push–pull resonant generator strongly depends on the operating frequency. As discussed in reference [42], the optimal operating condition is typically obtained at a frequency slightly lower than the resonance frequency of the generator–load system, in order to exploit the resonant voltage amplification while limiting switching losses.

As anticipated, actuator scaling significantly modifies the equivalent capacitance of the load. When increasing the actuator length from 5 cm to 200 cm, the equivalent capacitance increases by approximately a factor of 40 (from about 7.5 pF to 300 pF in plasma-off conditions and from about 15 pF to 600 pF in plasma-on conditions). According to:

$$f_{res} = \frac{1}{2\pi\sqrt{LC}}, \quad (3)$$

this increase in capacitance leads to a substantial reduction of the resonance frequency, where  $L$  is mainly determined by the inductive components of the generator and remains approximately constant during scaling.

The simulated frequency responses, reported in Figure 15, show that both the resonance frequency and the peak output voltage decrease when moving from the small to the large actuator. In plasma-off conditions, the resonance frequency shifts from approximately 32 kHz for the small reactor to about 16 kHz for the large reactor, while the maximum achievable output voltage (for constant DC bus voltage) decreases from approximately 8.5 kV to about 4 kV. When plasma ignition is considered, the additional plasma-related resistance further reduces both the resonance frequency and the peak voltage.

For the large-scale actuator in plasma-on conditions, the simulations predict a resonance frequency of approximately 12.5 kHz. This value is in good agreement with the experimental measurements, which show a resonance frequency close to 12 kHz (see Figure 14). Since the large actuator operates closer to the voltage limit of the generator, it becomes even more critical to operate very close to resonance in order to exploit the resonant voltage boost and ensure reliable plasma generation.

Finally, as reported in reference [43], a reduction of the operating frequency requires a higher voltage amplitude to maintain the same active power transferred to the discharge. Consequently, in order to correctly power the large-scale actuator (OPA-A) at its lower resonance frequency and guarantee a similar amount of thrust, the DC bus voltage of the generator was increased (and the operating point adjusted accordingly) to compensate for

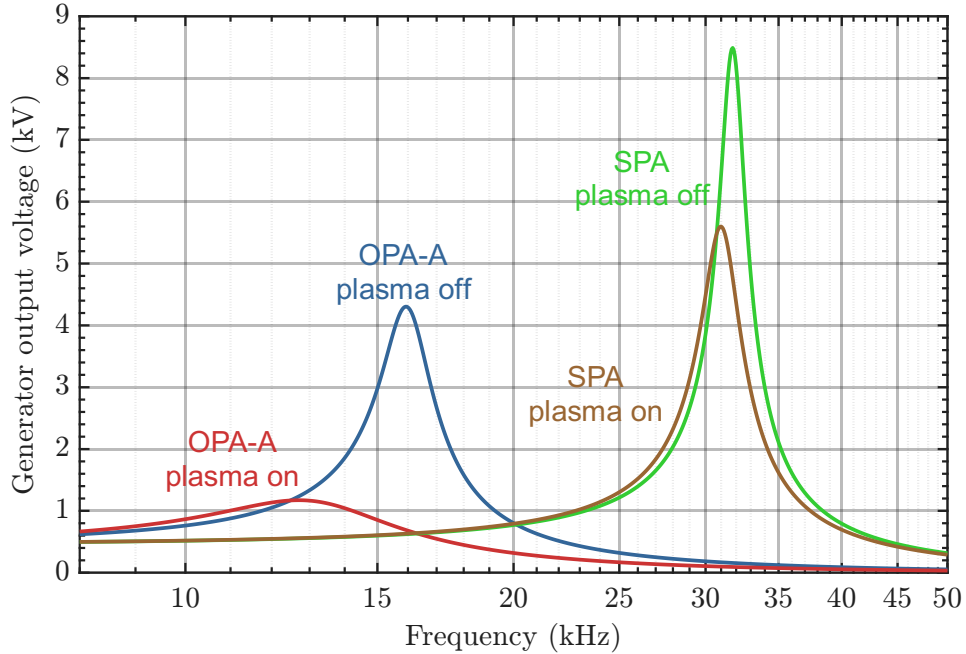


Figure 15: Frequency domain simulation (DC Bus voltage 10.8 V), single plasma actuator (SPA) vs oscillating plasma actuator array (OPA-A).

the reduced resonant gain and to preserve the desired specific average power delivered to the plasma.

As a final fluid-dynamic validation, the maximum induced velocity measured 2 mm downstream of the plasma edge at the wall ( $y = 0$ ) is reported in Figure 16 for both the large- and small-scale actuators as a function of the specific average power (the OPA-A being operated in unidirectional mode). The results show that the induced velocity produced by the OPA-A is comparable to that of the small-scale actuator. This confirms that the scaled power supply can properly drive the large-scale actuator and supports its use in the CICLoPE facility for future experiments.

## 5. Conclusions

This work presented the design, fabrication, and characterization of an array of oscillating plasma actuators (OPA-A) aimed at reproducing the effect of spanwise wall oscillations for turbulent skin-friction control. The actuator array offers a practical, non-mechanical solution to generate the wall-parallel oscillatory motions that have been shown to be effective in

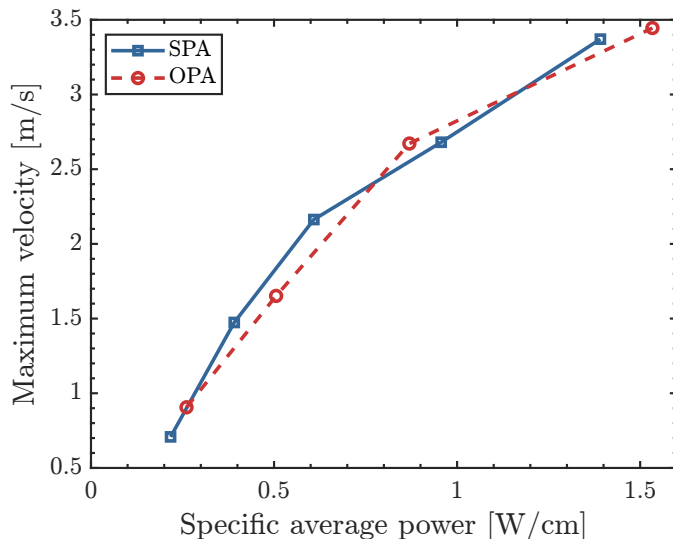


Figure 16: Maximum induced velocity as a function of the specific average power for the large-scale and lab-scale SPAs.

reducing turbulent friction drag. The transient behavior of the plasma-induced flow was investigated using high-speed Schlieren imaging, providing time- and space-resolved measurements of the evolving vortical structures. Unlike most previous experimental studies, which typically report phase-averaged velocity fields (e.g., obtained via planar or stereo PIV), the present approach resolves the instantaneous spatio-temporal dynamics of oscillating plasma actuators at modulation frequencies relevant to turbulence control. This enables direct characterization of the discharge-induced perturbation at time scales comparable to those of near-wall turbulent structures in high-Reynolds-number flows.

The actuators were shown to produce symmetric and repeatable spanwise jets with peak velocities of approximately 3.5 m/s at 4.5 kV, comparable to near-wall turbulence velocities. Electrical and thermal measurements confirmed stable operation within safe limits, with maximum surface temperatures kept below 110 °C to ensure durability.

The design was then scaled up and integrated with dedicated power electronics to allow operation at much larger dimensions. Tests demonstrated that a 2 m-long actuator can be powered effectively while maintaining performance, enabling future experiments in the CICLoPE Long Pipe facility at Reynolds numbers representative of aeronautical applications. The results presented here define the design space and operating conditions of oscillating

plasma actuators and establish their potential for large-scale implementation.

Overall, this study establishes both the design principles and the experimental foundation for deploying oscillating plasma actuators in large-scale, high-Reynolds-number turbulent flows. These results represent a critical step toward the active control of skin-friction using plasma-based forcing and open new opportunities for energy-efficient drag reduction in transportation applications.

### Acknowledgments

This study was carried out within the "Wall-Turbulence Active Control" project – funded by European Union – Next Generation EU within the PRIN 2022 PNRR program (D.D.1409 del 14/09/2022 Ministero dell'Università e della Ricerca). This manuscript reflects only the authors' views and opinions and the Ministry cannot be considered responsible for them.

Furthermore, this work was carried out within the MOST – Sustainable Mobility National Research Center and received funding from the European Union Next-GenerationEU [PIANO NAZIONALE DI RIPRESA E RESILIENZA (PNRR) – MISSIONE 4 COMPONENTE 2, INVESTIMENTO 1.4 – D.D.1033 17/06/2022, CN00000023].

### Appendix A. Hot-front tracking

The flow generated by plasma actuators can be visualized by acquiring high-speed Schlieren images, and measured by tracking the front of air warmer than ambient air. Because of the configuration of the Schlieren imaging setup adopted for these experiments, bright areas correspond to positive horizontal density gradients, whereas negative horizontal gradients are visualized as darker areas. A background subtraction procedure was applied to the raw images, followed by a min-max normalization of the luminosity intensity values and a masking procedure to isolate the actuator surface. To retrieve a measure of the temperature-gradient (and thus density-gradient) field generated by the plasma discharge, each image was integrated in a direction perpendicular to the knife-edge orientation, i.e. along the  $x$  axis. Indeed, the light intensity collected by the high-speed camera is related to the air density, through the following formula:

$$I(x, y) \propto \int \left( \frac{\partial \rho(x, y, z)}{\partial x} + \frac{\partial \rho(x, y, z)}{\partial y} \right) dz \quad (\text{A.1})$$

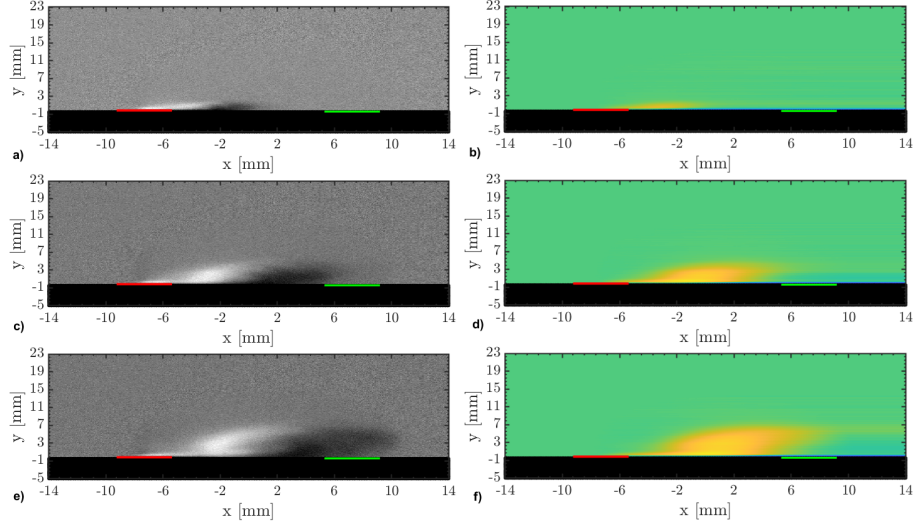


Figure A.1: Images taken at different actuation times (respectively 1.5, 5, 8 ms after operating HV 1). a,c,e): Images with background subtraction; b,d,f): Schlieren images after integration along the  $x$  axis.

Since the knife-edge was oriented along the  $y$  axis, the derivative of the density along this direction can be neglected; therefore, under the assumption of quasi 2-D velocity field, Equation (A.1) can be rewritten as:

$$I(x, y) \propto \Delta z \frac{\partial \rho(x, y)}{\partial x} \quad (\text{A.2})$$

Therefore, by integrating in the  $x$  direction the pixels counts in the Schlieren images, it is possible to retrieve a quantity which is related to the density gradient of the volume of air above the actuator surface.

$$\int_0^x I(x', y) dx' \propto \Delta z \int_0^x \frac{\partial \rho(x', y)}{\partial x'} dx' \quad (\text{A.3})$$

Since density gradients are generated by a temperature gradient, this quantity can be viewed as a measure of the temperature-gradient field above the actuator surface. The result is shown in Figure A.1. The first column of the figure shows images of the plasma-induced flow by HV 1 at different instants of time, after the background subtraction procedure. The second column represents the temperature gradient field produced by this induced flow, resulting from the integration procedure mentioned before.

Then, in order to create a robust hot-front tracking algorithm, the images were averaged column-wise: thus, a 2-D matrix of luminosity values is

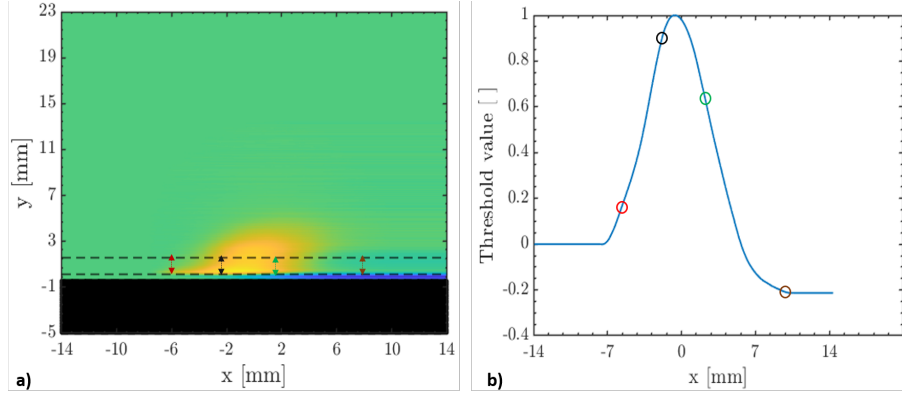


Figure A.2: (a) Example of a processed Schlieren image, with horizontal dashed lines as visual reference to show the restricted area over which the averaging procedure along the  $y$  axis is performed; (b) corresponding (normalized) horizontal temperature profile from integration of the results in the figure on the left.

reduced to a 1-D signal, and its evolution in time is analyzed to determine the hot-front displacement. Experiments have shown that a more reliable tracking is obtained by restricting the averaging operation only to a region very close to the actuator surface: this happens because, especially in the first instants after plasma ignition, the maximum of the temperature gradient lies in a very narrow region close to the dielectric. This operation is schematized in Figure A.2.

For the acquired snapshots, the PIF propagation front was identified using the following procedure:

1. Store global maximum ( $I_{max}$ ) and minimum ( $I_{min}$ ) signal values
2. Locate  $x_{max}$ , corresponding to  $I_{max}$
3. For  $x > x_{max}$ , define the front location ( $x_f$ ) as the  $x$  value where  $I = 0.7(I_{max} - I_{min})$

The employed 0.7 coefficient used for front tracking was determined empirically, seeking for the best front-evolution tracking along the  $x$  axis for the considered experiments.

## Appendix B. Vortex-core tracking

The flow induced by the plasma actuator entrains the adjacent fluid, generating a circulation that closes by continuity, thus forming a vortex. Therefore, an algorithm was developed capable of recognizing the vortical

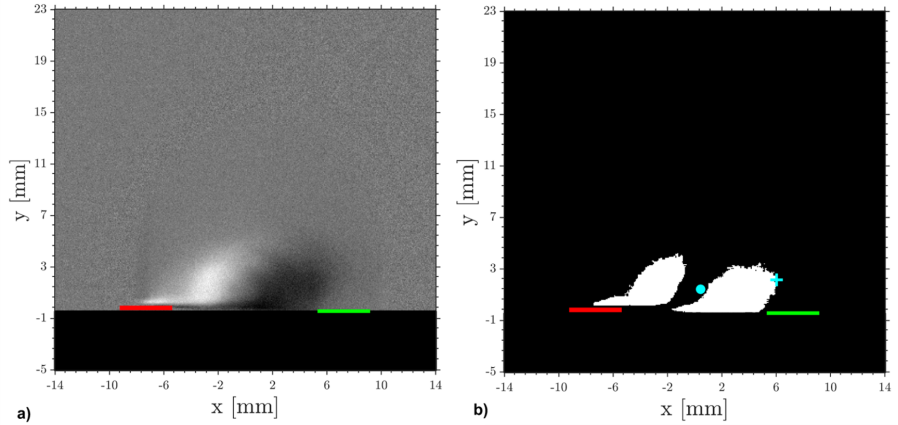


Figure B.1: a) Image of the vortex-core tracking produced by HV 1 after background subtraction; b) image resulting from the binarization procedure: the blue dot represents the vortex core, while the blue cross marks the vortex front.

structure, and then to track the evolution in time of its core displacement. This method allows to detect and track not only the displacement of the vortex core in the wall-parallel direction, but also in the wall-normal direction.

This procedure consists in the binarization of the pre-processed images based on a luminosity threshold value. The threshold criterion is not derived from a formal mathematical definition of a vortex core (e.g., based on velocity-gradient invariants), but rather from a qualitative visual identification of the vortex region, which is then translated into an automated intensity-based detection algorithm. Subsequently, the image is binarized as follows: a value of 1 is assigned only to those pixels whose intensity variation exceeds a given threshold, typically set to three standard deviations from the mean image intensity.

In principle, this operation allows to distinguish different vortical structures: either the ones associated to pixels brighter than the background image, or the ones formed by darker pixels than the background image, or one single (larger) vortical structure associated to those pixels whose intensity values have changed more than a given threshold, with respect to the background image.

After the binarization procedure, a median filter is applied to reduce the salt and pepper effect. The resulting image after these processing operations is shown in Figure B.1 b).

Then, it is possible to track both the displacement of the vortex front and the movement of the vortex core. The former is obtained by tracking

the coordinates of the outermost pixel (blue cross in Figure B.1 b), while the latter is determined by calculating the centroid of the two largest vortical structures, defined as the continuous set of all white pixels (blue dot in Figure B.1 b). This approach, applied to track the vortex core evolution, allows to detect displacements of the vortex core smaller than a single pixel, thereby increasing the accuracy of the measurement.

## References

- [1] P. Ricco, M. Skote, M. A. Leschziner, A review of turbulent skin-friction drag reduction by near-wall transverse forcing, *Progress in Aerospace Sciences* 123 (2021) 100713. doi:10.1016/J.PAEROSCI.2021.100713.
- [2] I. Ketut, I. K. Utama, B. Nugroho, R. Chin, M. Lukman, M. Hakim, F. Prasetyo, M. Yusuf, K. Suastika, J. Monty, N. Hutchins, B. Ganapathisubramani, A study of skin friction-drag from realistic roughness of a freshly cleaned and painted ship hull, in: *Proceedings of the International Symposium on Marine Engineering, ISME, 2017*, p. 6.
- [3] J. Schetz, Aerodynamics of high-speed trains, *Annual Review of Fluid Mechanics - ANNU REV FLUID MECH* 33 (2001) 371–414. doi:10.1146/annurev.fluid.33.1.371.
- [4] J. Kim, Physics and control of wall turbulence for drag reduction, *Philosophical Transactions of the Royal Society A: Mathematical, Physical and Engineering Sciences* 369 (2011) 1396–1411. doi:10.1098/rsta.2010.0360.
- [5] S. Ghaemi, Passive and active control of turbulent flows, *Physics of Fluids* 32 (2020) 10–12. doi:10.1063/5.0022548.
- [6] W. J. Jung, N. Mangiavacchi, R. Akhavan, Suppression of turbulence in wall-bounded flows by high-frequency spanwise oscillations, *Physics of Fluids A* 4 (1992) 1605–1607. doi:10.1063/1.858381.
- [7] K. S. Choi, M. Graham, Drag reduction of turbulent pipe flows by circular-wall oscillation, *Physics of Fluids* 10 (1998) 7–9. doi:10.1063/1.869538.
- [8] M. Quadrio, S. Sibilla, Numerical simulation of turbulent flow in a pipe oscillating around its axis, *Journal of Fluid Mechanics* 424 (2000) 217–241. doi:10.1017/S0022112000001889.

- [9] L. Agostini, E. Toubert, M. A. Leschziner, The turbulence vorticity as a window to the physics of friction-drag reduction by oscillatory wall motion, *International Journal of Heat and Fluid Flow* 51 (2015) 3–15. doi:10.1016/j.ijheatfluidflow.2014.08.002.
- [10] E. Moreau, Airflow control by non-thermal plasma actuators, *Journal of Physics D: Applied Physics* 40 (2007) 605–636. doi:10.1088/0022-3727/40/3/S01.
- [11] T. C. Corke, C. L. Enloe, S. P. Wilkinson, Dielectric barrier discharge plasma actuators for flow control, *Annual Review of Fluid Mechanics* 42 (2010) 505–529. doi:10.1146/annurev-fluid-121108-145550.
- [12] J. Kriegseis, B. Simon, S. Grundmann, Towards in-flight applications? a review on dielectric barrier discharge-based boundary-layer control, *Applied Mechanics Reviews* 68 (2016). doi:10.1115/1.4033570.
- [13] B. K. Mishra, P. K. Panigrahi, Formation and characterization of the vortices generated by a dbd plasma actuator in burst mode, *Physics of Fluids* 29 (2) (2017) 024104. doi:10.1063/1.4975156.
- [14] B. K. Mishra, P. K. Panigrahi, Dynamics and 3-d instability of flow induced by the dielectric-barrier-discharge plasma actuator in an initially quiescent medium, *Journal of Fluid Mechanics* 1008 (2025) A50. doi:10.1017/JFM.2025.198.
- [15] M. T. Hehner, D. Gatti, J. Kriegseis, Stokes-layer formation under absence of moving parts - a novel oscillatory plasma actuator design for turbulent drag reduction, *Physics of Fluids* 31 (2019) 1–6. doi:10.1063/1.5094388.
- [16] S. P. Wilkinson, Investigation of an oscillating surface plasma for turbulent drag reduction, 41st Aerospace Sciences Meeting and Exhibit (2003). doi:10.2514/6.2003-1023.
- [17] T. N. Jukes, K. S. Choi, G. A. Johnson, S. J. Scott, Turbulent drag reduction by surface plasma through spanwise flow oscillation, *Collection of Technical Papers - 3rd AIAA Flow Control Conference* 3 (2006) 1687–1700. doi:10.2514/6.2006-3693.
- [18] K.-S. Choi, T. Jukes, R. Whalley, Turbulent boundary-layer control with plasma actuators, *Philosophical Transactions of the Royal Society A: Mathematical, Physical and Engineering Sciences* 369 (2011) 1443–1458. doi:10.1098/RSTA.2010.0362.

- [19] R. D. Whalley, K. S. Choi, Turbulent boundary-layer control with plasma spanwise travelling waves, *Experiments in Fluids* 55 (2014). doi:10.1007/S00348-014-1796-3.
- [20] F. O. Thomas, T. C. Corke, A. Duong, S. Midya, K. Yates, Turbulent drag reduction using pulsed-dc plasma actuation, *Journal of Physics D: Applied Physics* 52 (2019). doi:10.1088/1361-6463/ab3388.
- [21] X. Q. Cheng, C. W. Wong, F. Hussain, W. Schröder, Y. Zhou, Flat plate drag reduction using plasma-generated streamwise vortices, *Journal of Fluid Mechanics* 918 (2021) 24. doi:10.1017/JFM.2021.311.
- [22] M. T. Hehner, L. H. von Deyn, J. Serpieri, S. Pasch, T. Reinheimer, D. Gatti, B. Frohnäpfel, J. Kriegseis, Stereo piv measurements of oscillatory plasma forcing in the cross-plane of a channel flow, 14th International Symposium on Particle Image Velocimetry 1 (8 2021). doi:10.18409/ISPIV.V1I1.117.
- [23] M. Abdullah, M. T. Galib, M. S. A. Khan, T. Rahman, M. M. Hosain, Recent advancements in flow control using plasma actuators and plasma vortex generators, *Heat Transfer* 53 (2024) 4244–4267. doi:10.1002/HTJ.23131.
- [24] J. Serpieri, M. T. Hehner, J. Kriegseis, Steady bi-dimensional crossflow plasma jets in turbulent channel flows, *Flow, Turbulence and Combustion* (2023) 1–17doi:10.1007/S10494-023-00463-W.
- [25] N. Benard, E. Moreau, J. P. Bonnet, Drag reduction by wall-parallel standing wave with plasma actuator, in: *AIAA SciTech Forum and Exposition, 2024*, American Institute of Aeronautics and Astronautics Inc, AIAA, 2024. doi:10.2514/6.2024-1512.
- [26] Z. Fang, H. Zong, X. Zhang, Y. Wu, Z. Su, H. Liang, D. Bian, Experimental investigation of a spanwise plasma jet array in a turbulent boundary layer for skin-friction drag reduction, *Physics of Fluids* 36 (10 2024). doi:10.1063/5.0226539.
- [27] F. M. Ricci, E. Amico, G. Cafiero, G. Iuso, J. Serpieri, Plasma jets in a turbulent channel flow, in: R. Örlü, A. Talamelli, J. Peinke, M. Oberlack (Eds.), *Progress in Turbulence X*, Springer Nature Switzerland, Cham, 2024, pp. 249–255. doi:10.1007/978-3-031-55924-2\_33.

- [28] J. Serpieri, G. Cafiero, G. Iuso, Conditioning turbulent channel flows with wall plasma jets, *AIAA Aviation Forum and ASCEND*, 2024 (2024). doi:10.2514/6.2024-4384.
- [29] X. Wei, Y. Zhou, Scaling of flat plate drag reduction using plasma-generated streamwise vortices, *Journal of Fluid Mechanics* 1007 (2025) R5. doi:10.1017/JFM.2025.116.
- [30] H. Zong, Z. Su, H. Liang, Y. Wu, Experimental investigation and reduced-order modeling of plasma jets in a turbulent boundary layer for skin-friction drag reduction, *Physics of Fluids* 34 (8 2022). doi:10.1063/5.0104609.
- [31] Z. Su, H. Zong, H. Liang, J. Li, Y. Wu, Optimization in frequency characteristics of an oscillating dielectric barrier discharge plasma actuator, *Sensors and Actuators A: Physical* 351 (2023) 114195. doi:https://doi.org/10.1016/j.sna.2023.114195.
- [32] W. Schoppa, F. Hussain, A large-scale control strategy for drag reduction in turbulent boundary layers, *Physics of Fluids* 10 (1998) 1049–1051. doi:10.1063/1.869789.
- [33] G. Iuso, M. Onorato, P. G. Spazzini, G. M. D. Cicca, Wall turbulence manipulation by large-scale streamwise vortices, *Journal of Fluid Mechanics* (2002). doi:10.1017/S0022112002002574.
- [34] J. Serpieri, M. Hehner, J. Kriegseis, Active electrode isolation for advanced plasma actuators, *Sensors and Actuators A: Physical* 343 (2022) 113675. doi:10.1016/J.SNA.2022.113675.
- [35] I. Marusic, D. Chandran, A. Rouhi, M. K. Fu, D. Wine, B. Holloway, D. Chung, A. J. Smits, An energy-efficient pathway to turbulent drag reduction, *Nature Communications* 12 (2021) 1–8. doi:10.1038/s41467-021-26128-8.
- [36] D. Chandran, A. Zampiron, A. Rouhi, M. fu, D. Wine, B. Holloway, A. Smits, I. Marusic, Turbulent drag reduction by spanwise wall forcing. part 2. high-reynolds-number experiments, *Journal of Fluid Mechanics* 968 (2023) 29. doi:10.1017/jfm.2023.498.
- [37] D. Gatti, M. Quadrio, A. Chiarini, F. Gattere, S. Pirozzoli, Turbulent skin-friction drag reduction via spanwise forcing at high reynolds number, *Journal of Fluid Mechanics* 1016 (2025) A58. doi:10.1017/JFM.2025.10412.

- [38] E.-S. Zanoun, C. Egbers, R. Örlü, T. Fiorini, G. Bellani, A. Talamelli, Experimental evaluation of the mean momentum and kinetic energy balance equations in turbulent pipe flows at high Reynolds number, *Journal of Turbulence* 20 (5) (2019) 1–15. doi:10.1080/14685248.2019.1628968.
- [39] G. Bellani, A. Talamelli, The Final Design of the Long Pipe in CIC-LOPE, *Springer Proceedings in Physics* (2016) 205–209doi:10.1007/978-3-319-29130-7\_36.
- [40] G. Neretti, A. Cristofolini, C. A. Borghi, Experimental investigation on a vectorized aerodynamic dielectric barrier discharge plasma actuator array, *Journal of Applied Physics* 115 (16) (2014).
- [41] A. Cristofolini, C. A. Borghi, G. Neretti, Charge distribution on the surface of a dielectric barrier discharge actuator for the fluid-dynamic control, *Journal of Applied Physics* 113 (14) (2013).
- [42] G. Neretti, M. Ricco, Self-tuning high-voltage and high-frequency sinusoidal power supply for dielectric barrier discharge plasma generation, *Electronics* 8 (10) (2019) 1137.
- [43] G. Neretti, A. Popoli, S. G. Scaltriti, A. Cristofolini, Real time power control in a high voltage power supply for dielectric barrier discharge reactors: Implementation strategy and load thermal analysis, *Electronics* 11 (10) (2022) 1536.
- [44] M. Holub, On the measurement of plasma power in atmospheric pressure dbd plasma reactors, *International Journal of Applied Electromagnetics and Mechanics* 39 (1-4) (2012) 81–87.
- [45] A. V. Pipa, et al., Experimental determination of dielectric barrier discharge capacitance, *Review of Scientific Instruments* 83 (7) (2012) 073506. doi:10.1063/1.4741496.
- [46] G. S. Settles, *Schlieren and shadowgraph techniques: visualizing phenomena in transparent media*, Springer Science & Business Media, 2001.
- [47] C. A. Borghi, A. Cristofolini, G. Grandi, G. Neretti, P. Seri, A plasma aerodynamic actuator supplied by a multilevel generator operating with different voltage waveforms, *Plasma Sources Science and Technology* 24 (4) (2015) 045018.
- [48] M. Bolitho, J. Jacob, Thrust Vectoring Flow Control Using Plasma Synthetic Jet Actuators. doi:10.2514/6.2008-1368.